NASA/TM-2017-219522

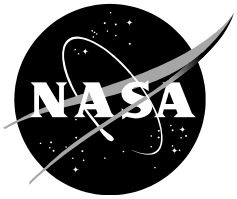

SHED VORTEX STRUCTURE AND PHASE-AVERAGED VELOCITY STATISTICS IN SYMMETRIC/ASYMMETRIC TURBULENT FLAT PLATE WAKES

*Man Mohan Rai**
Ames Research Center
Moffett Field, CA-94035

June 2017

* Senior Researcher, Computational Sciences, Exploration Technology Directorate.

NASA STI Program ... in Profile

Since its founding, NASA has been dedicated to the advancement of aeronautics and space science. The NASA scientific and technical information (STI) program plays a key part in helping NASA maintain this important role.

The NASA STI program operates under the auspices of the Agency Chief Information Officer. It collects, organizes, provides for archiving, and disseminates NASA's STI. The NASA STI program provides access to the NTRS Registered and its public interface, the NASA Technical Reports Server, thus providing one of the largest collections of aeronautical and space science STI in the world. Results are published in both non-NASA channels and by NASA in the NASA STI Report Series, which includes the following report types:

- TECHNICAL PUBLICATION. Reports of completed research or a major significant phase of research that present the results of NASA Programs and include extensive data or theoretical analysis. Includes compilations of significant scientific and technical data and information deemed to be of continuing reference value. NASA counterpart of peer-reviewed formal professional papers but has less stringent limitations on manuscript length and extent of graphic presentations.

- TECHNICAL MEMORANDUM. Scientific and technical findings that are preliminary or of specialized interest, e.g., quick release reports, working papers, and bibliographies that contain minimal annotation. Does not contain extensive analysis.

- CONTRACTOR REPORT. Scientific and technical findings by NASA-sponsored contractors and grantees.

- CONFERENCE PUBLICATION. Collected papers from scientific and technical conferences, symposia, seminars, or other meetings sponsored or co-sponsored by NASA.

- SPECIAL PUBLICATION. Scientific, technical, or historical information from NASA programs, projects, and missions, often concerned with subjects having substantial public interest.

- TECHNICAL TRANSLATION. English-language translations of foreign scientific and technical material pertinent to NASA's mission.

Specialized services also include organizing and publishing research results, distributing specialized research announcements and feeds, providing information desk and personal search support, and enabling data exchange services.

For more information about the NASA STI program, see the following:

- Access the NASA STI program home page at http://www.sti.nasa.gov

- E-mail your question to help@sti.nasa.gov

- Phone the NASA STI Information Desk at 757-864-9658

- Write to:
  NASA STI Information Desk
  Mail Stop 148
  NASA Langley Research Center
  Hampton, VA 23681-2199

NASA/TM-2017-219522

SHED VORTEX STRUCTURE AND PHASE-AVERAGED VELOCITY STATISTICS IN SYMMETRIC/ASYMMETRIC TURBULENT FLAT PLATE WAKES

Man Mohan Rai
Ames Research Center
Moffett Field, California

National Aeronautics and
Space Administration

Ames Research Center
Moffett Field, California 94035-1000

June 2017

SHED VORTEX STRUCTURE AND PHASE-AVERAGED VELOCITY STATISTICS IN SYMMETRIC/ASYMMETRIC TURBULENT FLAT PLATE WAKES

Man Mohan Rai*
NASA Ames Research Center, Moffett Field, CA-94035

ABSTRACT

The near wake of a flat plate is investigated via direct numerical simulations (DNS). Many earlier experimental investigations have used thin plates with sharp trailing edges and turbulent boundary layers to create the wake. This results in large θ/D_{TE} values (θ is the boundary layer momentum thickness towards the end of the plate and D_{TE} is the trailing edge thickness). In the present study the emphasis is on relatively thick plates with circular trailing edges (CTE) resulting in θ/D values less than one (D is the plate thickness and the diameter of the CTE), and vigorous vortex shedding. The Reynolds numbers based on the plate length and D are 1.255×10^6 and 10,000, respectively. Two cases are computed; one with turbulent boundary layers on both the upper and lower surfaces of the plate (statistically the same, symmetric wake, Case TT) and, a second with turbulent and laminar boundary layers on the upper and lower surfaces, respectively (asymmetric case, Case TL). The data and understanding obtained is of considerable engineering interest, particularly in turbomachinery where the pressure side of an airfoil can remain laminar or transitional because of a favorable pressure gradient and the suction side is turbulent. Shed-vortex structure and phase-averaged velocity statistics obtained in the two cases are compared here. The upper negative shed vortices in Case TL (turbulent separating boundary layer) are weaker than the lower positive ones (laminar separating boundary layer) at inception (a factor 1.27 weaker in terms of peak phase-averaged spanwise vorticity at first appearance of a peak). The upper vortices weaken rapidly as they travel downstream. A second feature of interest in Case TL is a considerable increase in the peak phase-averaged, streamwise normal intensity (random component) with increasing streamwise distance (x/D) that occurs nears the positive vortex cores. This behavior is observed for a few diameters in the near wake. This is counter to Case TT where the peak value essentially decreases with increasing x/D. Both these effects are examined in detail and the important contributors are identified.

INTRODUCTION

The near and intermediate wakes of airfoil sections used in turbomachinery are of considerable engineering importance. The near wake is of practical interest from the point of view of trailing edge design and the intermediate wake is of interest in understanding and predicting flow transition and unsteady loads on downstream airfoils. The magnitude of the coherent fluctuations due to vortex shedding, in particular fluctuations in the velocity and pressure, are of interest in determining the unsteady loads to be used in design.

---

* Senior Researcher, Computational Sciences, Exploration Technology Directorate.

A substantial amount of research has been conducted on cylinder wakes. Experimental techniques have generated a large percentage of the data that have provided us with the current state of understanding of the subject. More recently computational techniques, such as large eddy and direct numerical simulations have been used to compute cylinder wakes, and the data from such simulations are being used to refine our understanding of such flows and to obtain new insights. The physics of the very near wake of the cylinder (less than three diameters downstream) is perhaps the most challenging. This region comprises the two detached shear layers, the recirculation region and wake flow.

From an engineering point of view, there is considerable interest in the situation where the upper and/or lower boundary layer of an airfoil is turbulent, and these turbulent boundary layers separate from the airfoil to contribute to the formation of the wake downstream. In the case of cylinders of small diameter, this only occurs at relatively large unit Reynolds numbers. However, in the case of airfoils, the boundary layer has the opportunity to transition to turbulence on the airfoil surface at a substantially lower unit Reynolds number because the characteristic length of the airfoil is typically one to two orders of magnitude larger than the trailing edge diameter (this transition to turbulence would occur unless there is a strong favorable pressure gradient that results in the boundary layer remaining laminar or transitional over the surface of the airfoil). Unlike the cylinder, and more in keeping with the airfoil, a flat plate can have turbulent boundary layers for modest values of the unit Reynolds number without the accompanying complexities of the airfoil such as pressure gradients and geometry specificity. In addition, with a blunt trailing edge and an appropriate (θ/D) value, the plate will shed vortices vigorously. Hence the wake of the flat plate provides us with the opportunity to investigate the complexities of wake formation and evolution in the presence of turbulent separating boundary layers and vortex shedding in a relatively simple computational/experimental setting.

The majority of the published data for turbulent flat plate wakes that are preceded by turbulent boundary layers deals with thin plates. One of the earliest investigations in this area is by Chevray & Kovaznay. They provide measurements in the turbulent wake of a thin flat plate. The boundary layers at the end of the plate are fully turbulent. The ratio of the boundary layer momentum thickness to the trailing edge thickness of the plate (θ/D_{TE}) is 23.2. The thickness of the trailing edge in wall coordinates (based on the wall shear velocity at the end of the plate) is 3.0 and hence smaller than the viscous sub-layer. The turbulent boundary layers merge gradually to form the wake. Large scale Karman vortex formation is not observed in this situation. Experimental data provided in this study include mean velocity and turbulence intensity profiles at several streamwise locations along the wake. Other important contributions to the understanding of the wakes of thin plates with sharp trailing edges include those of Ramaprian et al (1982), Nakayama & Liu (1990) & Hayakawa & Iida (1992).

In many instances, unlike the plate experiments discussed above, the ratio of the momentum thickness of the boundary layer at the trailing edge to the trailing edge thickness is not large. For reasons of manufacturability, cost and reliability, the trailing edge thickness is larger than the boundary layer momentum thickness. Ratios (θ/D) close to or smaller than 1.0 are of interest from an engineering point of view. Here the boundary layers do not merge smoothly to form the wake as in the large θ/D case. Instead, large scale Karman vortex formation is present. Smaller scale turbulent structures are found embedded in the larger Karman vortices. Thus these wake flows share some attributes with the wakes that are obtained using flat plates with blunt trailing edges. A detailed investigation of the wake of the thick plate with a circular trailing edge and *turbulent separating boundary layers,* was initiated by Rai (2013, 2014 & 2015). This was accomplished with the aid of DNSs. The boundary layers as well as the wake were computed via DNS in these investigations. The separating boundary layers are fully turbulent well upstream of the trailing edge and are statistically identical. Thus the wake is symmetric in the mean.

In Rai (2013) distributions of the phase-averaged turbulent intensity and shear stress (random component) in the near wake are explored and compared with cylinder experimental data. Wherever possible a physical explanation of the origin of the important features of the distributions, as well as one based on the distribution of the production term in the corresponding budget, is provided. A new event-

based phase-averaging procedure is introduced. Some of the important features of the near wake, such as the strength and structure of rib vortices in relation to the shed vortices, their evolution in time, the internal structure of shed vortices etc. are investigated here. Some of the findings are as expected (rib vortices in the braids) while others such as the presence of intense elongated spanwise vortices instead of a single columnar vortex in the cores provide new understanding of the cores and braids and the interaction between them.

In Rai (2014) the emphasis is on the stability of the detached shear layers, rib-vortex induced reverse flow, and phase-averaged distributions of the random component of normal intensities and shear stress and the production term in the corresponding budgets in the *very* near wake ($x/D < 3.0$). It was determined that, as in the case of the cylinder with laminar separating boundary layers, the flat plate wake also exhibits shear layer instability followed by the formation of shear layer vortices that have a profound impact on the structure of the shear layer and the formation of the shed vortices. However, unlike the cylinder case, here only a small fraction of the separated turbulent boundary layer participates in the initial formation of the shed vortices and, it is this fraction that is unstable. An examination of the distribution of streamwise velocity in the wake center-plane (Rai, 2014) first led to the discovery of regions of isolated reverse flow that are disconnected from the main body of reverse flow in the trailing edge region. They are first formed near the trailing edge and convect downstream. These regions are a result of powerful rib vortices that are formed in the high-strain-rate region that exists between the shed vortices in their initial state; the rib vortices can be quite powerful with streamwise velocities (negative) within them reaching 40% of the freestream velocity. They are accompanied by pressure minima and relatively high cross-stream vorticity levels and are observed as far downstream as $x/D = 4.0$.

In Rai (2015) the emphasis is on entrainment and the instability of the detached shear layers. As mentioned earlier only a small fraction of the separating turbulent boundary layer forms the detached shear layer and participates in the initial roll-up into the shed vortex. A natural consequence of this behavior is that for some distance downstream the wake with its shed vortices ingests fluid that was originally part of the turbulent boundary layer. The log-layer eddies are assimilated in this process and become a part of the shed vortices or the braids; a visualization is provided in the article. An investigation of the effect of increasing θ/D on assimilation/entrainment is also provided. It clearly shows that wakes with larger θ/D values continue to assimilate boundary layer fluid for longer (until a larger value of x/D); the important contributors to this effect are identified. The study also shows that wake TKE profiles, in the region away from the shed vortices and braids, are close to that of the upstream turbulent boundary layer (especially in the very near wake for the large θ/D cases). This again is a consequence of the fact that much of the turbulent boundary layer does not participate in the initial shed-vortex roll-up process. A visualization of shear-layer instability events in a (t, z) plane in Rai (2015) showed that shear-layer vortex generation rates can vary as much as a factor of two from event to event. An analysis of velocity fluctuations in the upstream boundary layer indicated that high-speed streaks near the trailing edge result in higher shear-layer vortex generation rates.

The emphasis in the present study is the asymmetric shedding wake. There are a few earlier investigations of asymmetric wakes in the literature. Thomas & Liu (2004) report on an experimental investigation of symmetric and asymmetric turbulent wakes behind a flat plate. The thickness of the plate is tapered down to 1.6 mm at a taper angle of 2.2^o in the last 0.2 meters of the plate length. Hence as in earlier flat plate wake experiments the value of θ/D_{TE} is large and little or no shedding is expected. The asymmetric wake is obtained by introducing a semicircular bump on the lower side and a suction slot on the upper side of the plate. The net effect is a θ_L/θ_U ratio of 2.5. Data are provided for adverse, favorable and zero pressure-gradient wakes (APG, FPG and ZPG, respectively).

Some of the principal findings of the study by Thomas & Liu (2004) for the ZPG case are, 1) a cross-stream migration (downward towards the thicker side of the wake) of the location of the maximum local velocity defect with streamwise distance and more rapid wake spreading in the asymmetric case, 2) the velocity defect decay rate for both the symmetric and asymmetric cases were found to be nearly the

same and close to a $x^{-1/2}$ variation, and, 3) a trend toward symmetric velocity profiles downstream in the asymmetric case. Velocity defect profiles for the symmetric case showed excellent similarity while the asymmetric profiles collapsed reasonably well although not quite symmetric about the centerline. The cross-stream distance in the asymmetric case was measured from the location at which maximum velocity defect occurs, and it was normalized by the respective wake thickness (upper and lower).

Hah & Lakshminarayana (1982) provide experimentally obtained asymmetric airfoil wake data. Asymmetry was achieved via three positive incidence angles. The suction side exhibits a thicker boundary layer than the pressure side. This study, as in the previous one examines a flow where trailing edge shedding is minimal. Data in the near and intermediate regions of the wake including cross-stream profiles of velocity, turbulence intensities and Reynolds shear stress are analyzed. The mean velocity profiles were found to be nearly symmetric at 1.5 chords downstream of the trailing edge even though they are significantly asymmetric initially. When normalized with the defect velocity and respective wake half-thickness values, the velocity profiles exhibited similarity and proximity to a Gaussian distribution except in the very near wake particularly in the outer wake region. The authors observe that for the very near wake, inner scales are more appropriate than the outer scales that are employed in exploring similarity. Wake width (with an accommodation for changing drag coefficient) was found to vary as the square root of the streamwise distance from the trailing edge and, the centerline velocity in the intermediate wake according to the log-law (as has been observed for flat plate wakes). Turbulent normal intensity profiles were also found to become fairly symmetric at 1.5 chords from the trailing edge. When normalized by the *local* maximum intensity, and length scales corresponding to the half width of the *intensity profiles*, these profiles also collapsed reasonably well. However, fairly large deviations from a Gaussian function were observed in the very near wake and in the outer region of the wake. Reynolds shear stress profiles were found to achieve shape similarity at 1.5 chords but peak magnitudes on the suction and pressure sides were substantially different. The shear stress was slower in achieving similarity than the normal intensities.

The objective of the present study is to understand the differences in the near wake physics of symmetric (Case TT) and asymmetric (Case TL) wakes of a flat plate with a circular trailing edge exhibiting vigorous vortex shedding. Data from direct numerical simulations (DNS) are utilized here. The asymmetry in the latter case is obtained via a turbulent separating boundary layer on the upper surface of the plate and a laminar one on the lower surface. Differences in shed vortex structure/strength and phase-averaged velocity statistics are investigated in the near wake ($x/D < 13.0$).

FLAT-PLATE COMPUTATIONAL GRID, FLOW/GEOMETRY PARAMETERS AND NUMERICAL METHOD

The computational region for the flat plate DNSs is divided into two zones to facilitate grid generation and provide adequate grid resolution for the wake. Figure 1 shows the plate cross-section and the two zones that comprise the computational region. The three-dimensional zones and grids are obtained by uniformly spacing copies of these two-dimensional zones in the spanwise direction (z). The plate zone is bounded by four boundaries: the plate surface (excluding the trailing edge), an external boundary and, two zonal boundaries (top and bottom) that interface with the wake zone. The plate zone captures the flow-field upstream of the trailing edge including the plate boundary layers. The leading edge of the plate is an ellipse. The wake zone is constructed to provide adequate grid resolution for the detached shear layers, the recirculation region and the wake. The boundaries of this zone include the circular trailing edge, the upper and lower boundaries and the exit boundary. Both the upper and lower boundaries consist of a zonal boundary segment that interfaces with the plate zone and a second segment that serves as an external boundary.

The present Case TT is the same as Case A in Rai (2013, 2014 & 2015). Only Case TL was computed as a part of the current study. The placement of the various boundaries in relation to the plate

surface in Case TT (Case A) is provided in Rai (2013, 2014 & 2015). The vertical extent of the wake zone near the trailing edge, where its upper/lower boundaries are horizontal is large enough to completely contain the wake in all cases (Fig. 4 in Rai 2013 clearly shows the adequacy of this dimension in Case A). The spanwise extent of the computational domain in Case A is 4.0D.

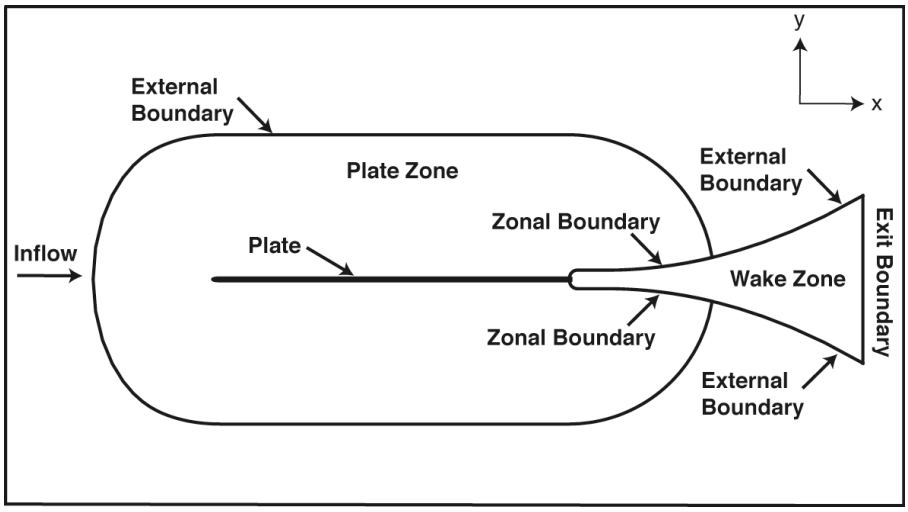

Figure 1. Midspan plate section and multiple zone discretization of the computational region (Rai 2013).

Figure 2 shows representative grids in the vicinity of the trailing edge in both zones. Both the grids have the same spacing in the wall normal direction at the plate surface. Downstream of the region of interest ($x/D \approx 13.5$), the wake grid coarsens gradually in the x direction. This coarsening reduces computational costs and dissipates the wake to a degree that inviscid exit boundary conditions can be employed at the exit boundary of the wake zone.

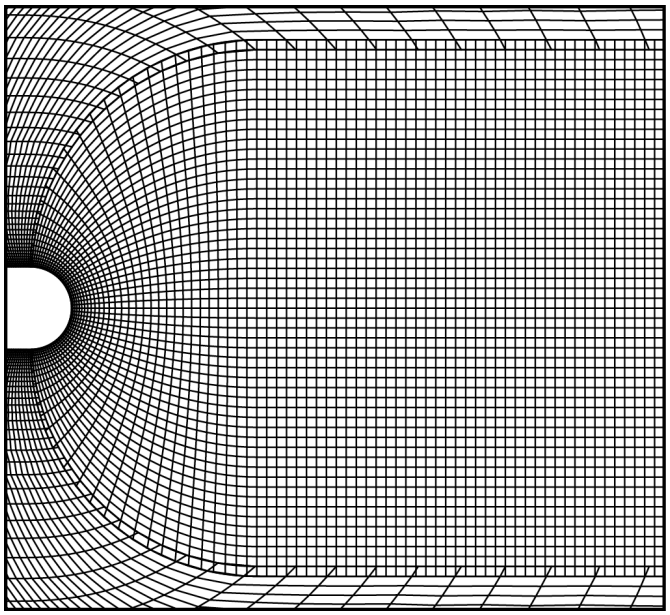

Figure 2. Representative grids in the plate and wake zones in the trailing edge region (Rai 2013).

The wake grid for Case TT was constructed with 741 grid points in the streamwise direction, 411 in the cross-stream direction and 256 in the spanwise direction (about 78 x 10^6 grid points). The resolution

achieved along the centerline in the three spatial directions at x/D = 10.0 is approximately $\Delta x/\eta = 3.7$, $\Delta y/\eta = 2.2$ and $\Delta z/\eta = 2.1$ where η is the computed Kolmogorov length scale at the same location. The grid resolution in the plate grid in the x, y and z directions for this case is about 17.8, 0.84 and 6.6 wall units respectively, based on the wall shear velocity near the end of the plate. The adequacy of the grid resolution and domain size used is demonstrated in Rai (2013 & 2014). A comparison of computed boundary layer turbulent intensities with experimental data is provided in Rai (2013). The computations are performed at a Mach number of 0.2. *The computational domain and grid used to compute Case TL is identical to that used in Case TT.*

A high-order accurate upwind-biased method is used here to compute the flow over the plate as well as that in the wake. The convective terms are computed using sixth- and seventh-order upwind-biased finite differences, both with seventh-order dissipation terms. The viscous terms are computed with fourth-order central differences. The method is iterative-implicit in nature, multiple iterations are employed at each time-step to solve the nonlinear finite-difference equations arising from a fully implicit formulation; the method is second-order accurate in time. The boundaries that contain the computational grids can be classified as natural and zonal boundaries. The natural boundaries include the external boundary of the plate grid, the surface of the plate, the exit boundary of the wake grid, the segments of the upper and lower boundaries of the wake grid labeled as “external boundary” in Fig. 1, and, the boundaries in the *z* direction. The upstream segment of the upper boundary between the plate and wake grids is an example of the zonal boundaries used in the computation. Periodic boundary conditions are imposed on the boundaries in the *z* direction (homogeneity in *z*). No-slip/adiabatic wall conditions are used on the plate surface. Wall blowing/suction is implemented on a short segment of the upper surface of the plate (and lower surface in Case TT) to induce boundary layer transition to turbulence; flow transition occurs well upstream of the trailing edge. The transitional/turbulent boundary layers and the wake are all computed via DNS. The natural and zonal boundary conditions, and the high-order accurate upwind-biased finite-difference method used here are discussed in detail in the author’s earlier articles cited in Rai (2015).

RESULTS

The plate computations were performed at a Mach number of 0.2. The Reynolds number based on the diameter, and plate length, are 10,000 and 1,255,000, respectively. The initial transients were eliminated by integrating the governing equations over a period corresponding to a large number of trailing edge vortex-shedding periods. The time step in both cases was the same. The computed Strouhal numbers in Cases TT and TL are 0.173 & 0.205, respectively.

In the following contour plots the colors blue/green represent negative values (deep blue representing the lowest value) of the term/quantity being discussed. Orange, red and magenta represent positive values (magenta bordering on white representing the highest value). Shades of yellow represent values close to zero. In figures containing multiple subplots of contours, the minimum and maximum value specified and, the increment between consecutive contour values is the same. Thus contours/features in the subplots can be directly compared.

Figures 3a & 3b, showing contours of instantaneous spanwise velocity in the trailing edge region for Cases TT & TL, respectively, are provided as an introduction to the symmetric and asymmetric flat plate wakes. Spanwise velocity fluctuations are an excellent indicator of the three-dimensionality of the turbulent boundary layer and wake in these two cases where the mean flow is two-dimensional. The lower shed vortices in Case TL are evident in Fig. 3b. The signature of the rib vortices in the region between shed vortices (long thin structures, one of them is shown in Fig.3a, blue arrow) can be discerned. The clear demarcation between the wakes and the outer flow in both the cases is also evident. Of particular interest to this study is the turbulent nature of the both the upper & lower boundary layers in Fig. 3a (Case TT) and turbulent/laminar boundary layer combination in Fig. 3b (Case TL, the lower laminar boundary does not exhibit spanwise velocity fluctuations).

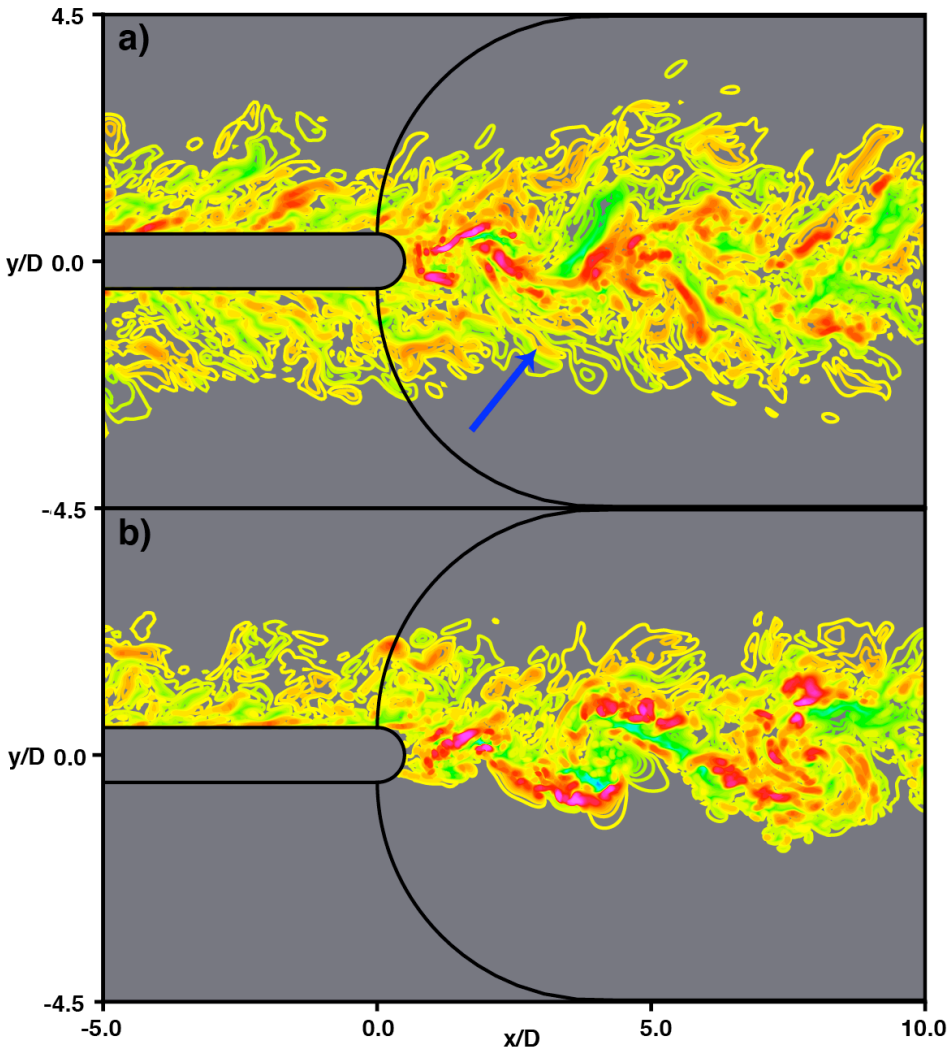

Figure 3. Contours of instantaneous spanwise velocity in an (x, y) plane a) Case TT b) Case TL: red/magenta represent high/highest positive values, green/blue low/lowest negative values, yellow ≈ 0.0.

Phase-Averaged Turbulence Statistics

The fluctuating density, pressure and velocity components in the flow field are assumed to contain a mean component, a periodic component at shedding frequency ω_{st} (and harmonics thereof), and a random turbulent component as in Reynolds & Hussain (1972). Thus a flow variable *q* is written as

$$q = \overline{q} + q' + q'' \qquad (1)$$

where $\overline{q}$ is the mean value, and q' and q'' are the random and periodic fluctuating components, respectively. The phase-averaged value $< q >$ (average at constant phase) is given by

$$<q(\phi)> = \overline{q} + q''(\phi) \qquad (2)$$

where ϕ is the phase, $0.0 \le \phi \le 1.0$. Phase-averaged turbulence statistics are computed by averaging the computed data both at constant phase and in the spanwise direction (since the flow is homogeneous

in this direction) and are obtained over approximately 160 shedding periods in both cases. The phase-averaging method used here is described in Appendix B of Rai (2013).

One of the objectives of the present study is to better understand the observed distribution of the normal intensities and shear stress (random component) in the braid and vortex core regions. For that we will resort to the budget of the phase-averaged turbulent stresses (Rai, 2012) later in the text. The incompressible form of the transport equations for the these stresses are obtained as

$$\rho\frac{\mathrm{D}<u_i'u_j'>}{\mathrm{Dt}} = \mathrm{P_{ij}} + \mathrm{T_{ij}} + \Pi_{ij} + \mathrm{D_{ij}} - \varepsilon_{ij} \qquad (3)$$

where ρ is the density and

$$\frac{\mathrm{D}<u_i'u_j'>}{\mathrm{Dt}} = \frac{\partial<u_i'u_j'>}{\partial t} + <u_k>\frac{\partial<u_i'u_j'>}{\partial x_k}$$

$$\mathrm{P_{ij}} = -\rho\left(<u_j'u_k'>\frac{\partial<u_i>}{\partial x_k} + <u_i'u_k'>\frac{\partial<u_j>}{\partial x_k}\right) \qquad \text{production rate}$$

$$\mathrm{T_{ij}} = -\rho\left(\frac{\partial<u_i'u_j'u_k'>}{\partial x_k}\right) \qquad \text{turbulent transport rate}$$

$$\Pi_{ij} = -<u_j'\frac{\partial p'}{\partial x_i} + u_i'\frac{\partial p'}{\partial x_j}> \qquad \text{velocity pressure-gradient term}$$

$$\mathrm{D_{ij}} = \mu\nabla^2<u_i'u_j'> \qquad \text{viscous diffusion rate}$$

$$\varepsilon_{ij} = 2\mu<\frac{\partial u_i'}{\partial x_k}\frac{\partial u_j'}{\partial x_k}> \qquad \text{dissipation rate} \qquad (4)$$

In Eqs. 3 & 4, p is the pressure, u_i (**i** = 1, 2, 3) are the velocity components in the streamwise, cross-stream and spanwise directions (x_i), μ is the viscosity of the fluid and repeated indices denote summation. The budget terms are similar to the ones obtained via time-averages as in Mansour, Kim & Moin (1988). Assuming the periodic fluctuations to be zero and replacing the phase-averaged quantities with their time-averaged counterparts in Eqs. 3 & 4 yields the formulation of Mansour, Kim & Moin (1988). As observed in their article, the velocity pressure-gradient term can be split into a pressure transport term and a pressure strain term; this is achieved here as well to yield

$$\Pi_{ij} = -\left(\frac{\partial<p'u_j'>}{\partial x_i} + \frac{\partial<p'u_i'>}{\partial x_j}\right) + \left(<\frac{p'\partial u_j'}{\partial x_i}> + <\frac{p'\partial u_i'}{\partial x_j}>\right) \qquad (5)$$

The turbulent diffusion terms are more than order of magnitude smaller than the other terms and are hence not discussed here.

A Comparison of Shed-Vortex Structure/Strength in Cases TT & TL

Contours of phase-averaged spanwise vorticity for Cases TT & TL are shown in Fig. 4 (vorticity has been filtered with a three-point filter to reduce high-frequency oscillations in the contours). Figure 4a shows contours for Case TT when the lower vortex core is at x/D = 5.5. Figures 4b & 4c show contours for Case TL when the lower and upper cores occupy the same streamwise location, respectively.

The streamwise evolution of the shed vortices in the two cases is better understood by examining the ratio of the magnitude of peak phase-averaged vorticity of relevant pairs of vortices of interest. Table 1 provides these ratios. Ratio # 1 (0.95) is close to unity.

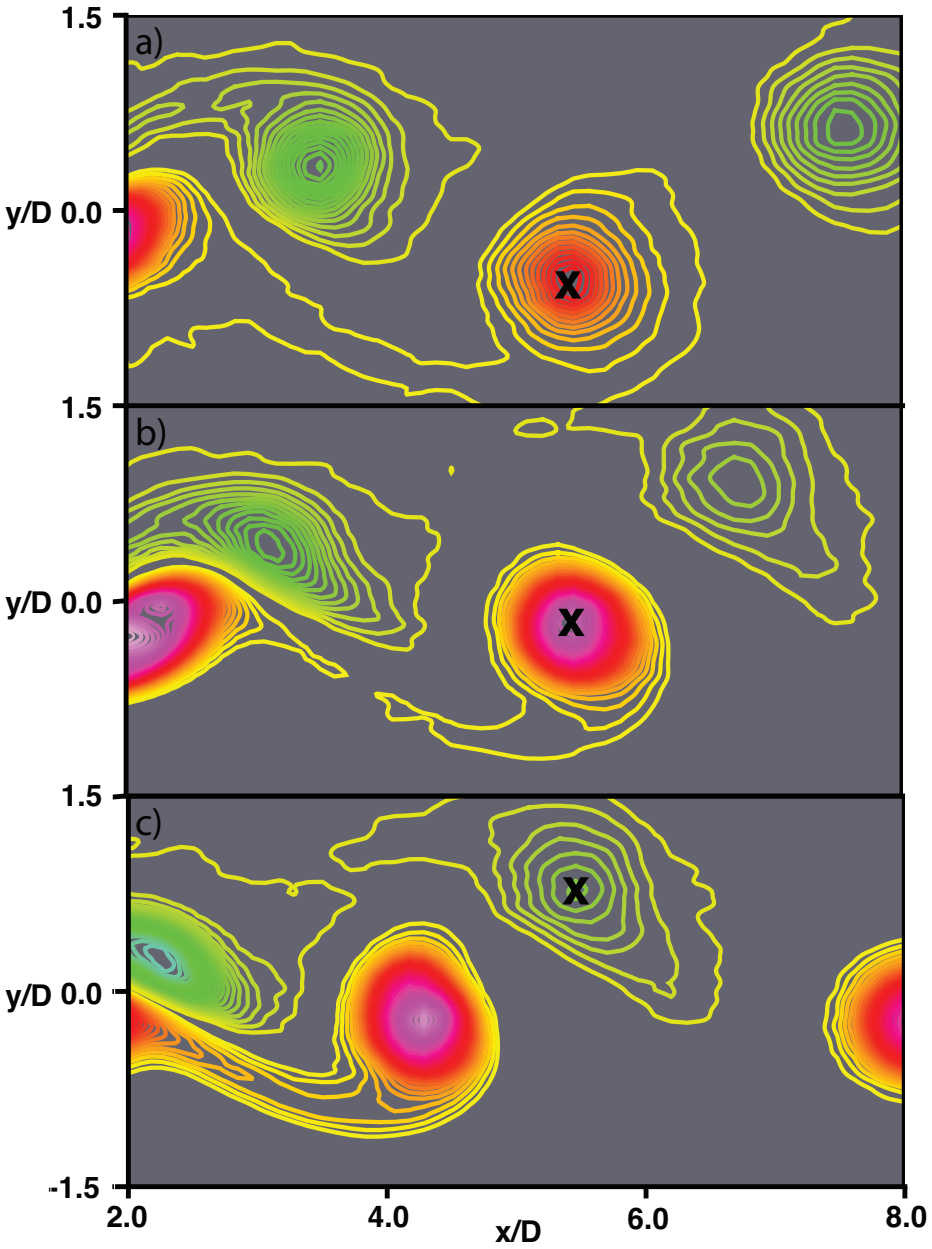

Figure 4. Contours of phase-averaged spanwise vorticity, 'X' marks the location of the vortex of interest at x/D = 5.5: a) Case TT (lower positive vortex), b) Case TL (lower positive vortex) and c) Case TL (upper negative vortex); red/magenta represent high/highest positive values, green/blue low/lowest negative values, yellow ≈ 0.0.

This is the ratio of peak vorticity obtained in the upper vortices in cases TL & TT at inception (inception is defined as when the peak in phase-averaged spanwise vorticity first appears). The proximity to 1.0 is to be expected since the boundary layer is turbulent in both cases and is nearly the same (velocity statistics upstream of the trailing edge). Ratio # 2 (1.27) indicates a more powerful lower vortex than the upper one at inception in Case TL. Ratio # 3 (1.21) shows that the lower vortex in Case TL is more powerful than its counterpart in Case TT, both at inception. Ratio # 4 (0.49) shows that during the travel from inception point (x/D = 1.09) to the downstream location x/D = 5.5, the upper vortex in Case TL weakens considerably more than its counterpart in Case TT (ratio decrease from 0.95 to 0.49). Ratio # 5 (3.45) shows extreme weakening of the upper vortex in Case TL when compared to the lower vortex in Case TL

(ratio increase from 1.27 to 3.45). Ratio # 6 (1.69) shows that the shed vortices in Case TT weaken in relation to the lower one in Case TL as they travel from the point of inception to x/D = 5.5 (increase in ratio from 1.21 to 1.69).

Ratio #	Vortex A of interest	Vortex B of interest	Ratio (A/B)
1)	Upper vortex, inception, x/D = 1.09, Case TL	Lower/upper vortex, inception, x/D = 0.99, Case TT	0.95
2)	Lower vortex, inception, x/D = 1.05, Case TL	Upper vortex, inception, x/D = 1.09, Case TL	1.27
3)	Lower vortex, inception, x/D = 1.05, Case TL	Lower/upper vortex, inception, x/D = 0.99, Case TT	1.21
4)	Upper vortex, x/D = 5.5, Case TL	Lower/upper vortex, x/D = 5.5, Case TT	0.49
5)	Lower vortex, x/D = 5.5, Case TL	Upper vortex, x/D = 5.5, Case TL	3.45
6)	Lower vortex, x/D = 5.5, Case TL	Lower/upper vortex, x/D = 5.5, Case TT	1.69

Table 1. Ratios of magnitude of peak phase-averaged spanwise vorticity associated with various pairs of vortices at locations of interest.

The questions that arise from the ratios provided above are as follows: Given that the upper boundary layer is turbulent in both cases and is nearly the same why is the peak negative vorticity (upper vortex) in Case TL less than half that obtained in Case TT at x/D = 5.5? *This is particularly interesting given that at inception the upper vortices in both cases have nearly the same peak vorticity (ratio of 0.95, TL/TT).* A related question is as follows: why is the lower vortex so much more powerful than the upper one in Case TL at x/D = 5.5, given that the initial ratio for these two vortices is 1.27 (evolves into 3.45)? Secondly, why is the lower positive vortex at inception in Case TL stronger than both its counterpart in Case TT (1.21, TL/TT) and the upper vortex in Case TL (1.27, lower/upper, Case TL)? Thirdly, why is the lower vortex in Case TL better preserved than in Case TT (the ratio TL/TT increases from 1.21 to 1.69)?

Figures 5a & 5b show contours of instantaneous spanwise vorticity for Case TT and TL, respectively. Both figures show the formation of the lower positive vortex and the inception of the upper negative vortex (all vortices marked with an 'X'). The highly fragmented nature of the lower detached shear layer (DSL) that is in the process of rolling up to form the lower vortex in Fig. 5a is apparent. Fragmentation is largely a result of the DSL instability. In addition, the lower vortex in Fig. 5a contains regions of both positive and negative vorticity with the regions of positive vorticity dominating. Here and later in the text, we will refer to this phenomenon where regions of negative vorticity are embedded in positive vortices and vice versa as 'vortex contamination' or simply 'contamination'. As seen in Fig. 5b, the lower DSL (laminar separating boundary layer) that is in the process of rolling up is less fragmented and the corresponding vortex shows a lower level of contamination. Contamination levels are higher further downstream even in Case TL as seen from the positive vortex downstream in Fig. 5b, at about x/D = 4.0; the shape of this vortex, however, is better preserved than its counterpart in Fig. 5a.

Another point of interest with regard to the initial roll-up of the DSL is that when the separating boundary layer is turbulent only a small fraction of the boundary layer (less than 35 wall units above the wall in Case TT) rolls up into the shed vortex (Fig. 4, Rai, 2014). The log-layer eddies convect past the trailing edge largely unaltered. Thus only a fraction of the boundary layer vorticity (accumulated over one shedding period) is contained in the shed vortex. When the separating plate boundary layer is laminar a large percentage of the vorticity in the separating boundary layer was found to accumulate in the shed

vortex in the flat plate case investigated in Rai (2014, Fig. 25). These two features can be observed in Figs. 5a & 5b as well. The convection of the log-layer eddies past the trailing edge, without being assimilated by the developing shed vortices, above and below the centerline in Fig. 5a and above the centerline in Fig. 5b is evident. The accumulation of most of the vorticity associated with the lower laminar boundary layer (in the shed vortex) is also evident in Fig. 5b.

Vortex contamination, DSL fragmentation, the vorticity contained within the boundary layer (profile integral), and the extent to which the boundary layer participates in the initial shed vortex formation process are all factors that affect the peak phase-averaged spanwise vorticity of the initial shed vortex. Vortex contamination and DSL fragmentation assert themselves in the phase-averaging process (averaging in z and constant phase) and the last two items via the total shed-vortex bound vorticity. An exhaustive study of the relative importance of these factors in defining the strength of the shed vortex is beyond the scope of the current study. However, as a consequence, in Case TL the lower shed vortex is stronger than the upper one and this has a profound effect on the development of the wake. The effect of a stronger lower shed vortex on the development of the weaker upper shed vortex is explored below.

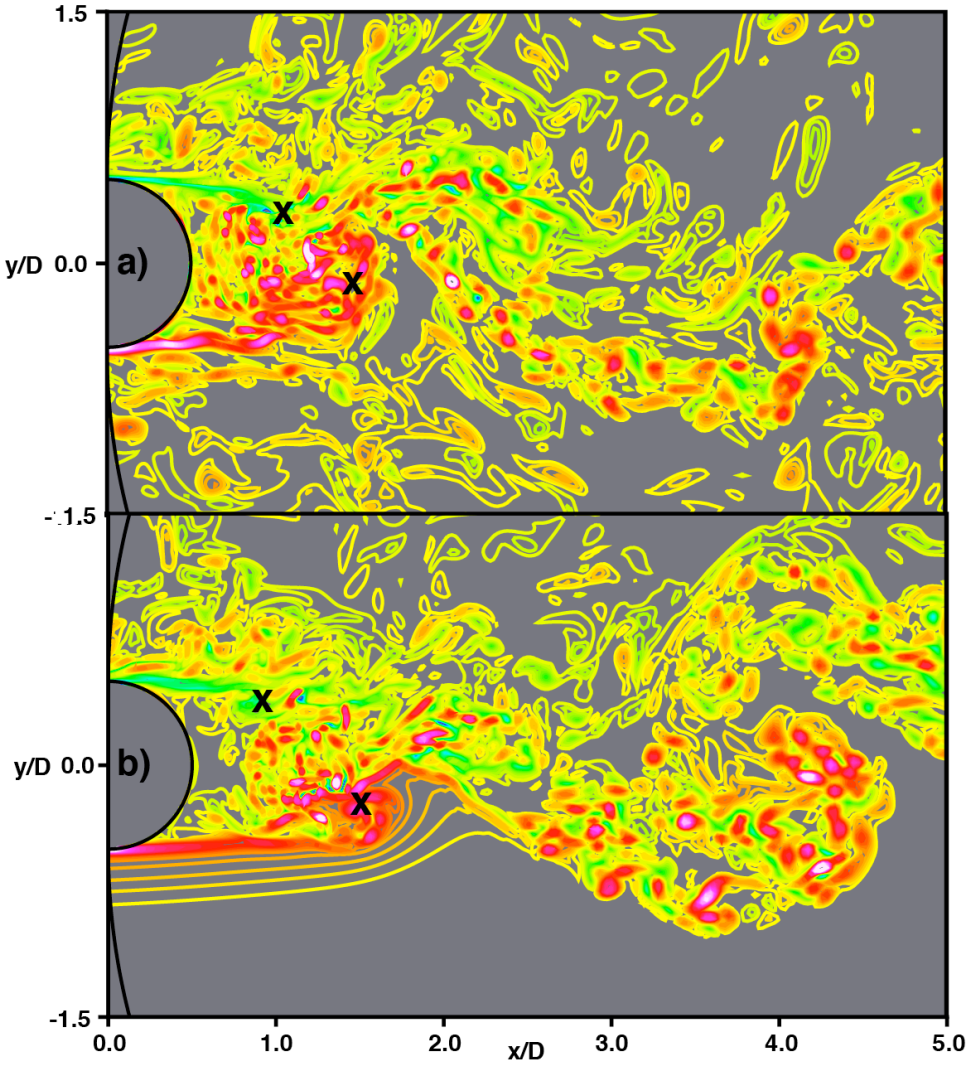

Figure 5. Contours of instantaneous spanwise vorticity in an (x, y) plane showing formation of lower positive shed vortex a) Case TT & b) Case TL; red/magenta represent high/highest positive values, green/blue low/lowest negative values, yellow ≈ 0.0.

Figures 6a & 6b show contours of instantaneous spanwise vorticity at two instants in time for Case TL. Both figures show an upper negative shed vortex (UNSV) and a lower positive shed vortex (LPSV). The approximate centers of these vortices, obtained via z-averaged pressure contours, are marked with an 'X'. Figure 6a shows three smaller 'constituent' regions of negative vorticity (A, B & C). Regions B and C are seen to be associated with the UNSV; region A is in close proximity to the UNSV but within the braid connecting the UNSV and LPSV. Figure 6b shows vorticity contours several time steps later. The LPSV has travelled about 0.8D downstream during this period. Figure 6b also shows the same three constituent regions of vorticity (A, B & C). However, at this point in time they are embedded in the LPSV. The LPSV has essentially acquired the constituent regions of negative vorticity of the UNSV. This is not an isolated incident. Animations show that the more powerful LPSV rapidly accumulates the constituent negative regions of vorticity of the UNSV. The accumulation process is more rapid when the shed vortices are just formed and are in close proximity to each other. The end effect of this loss of negative vorticity from the UNSV to the LPSV is a weakening of both the shed vortices. In a relative sense, the UNSV suffers more from this effect than the LPSV because the LPSV is stronger.

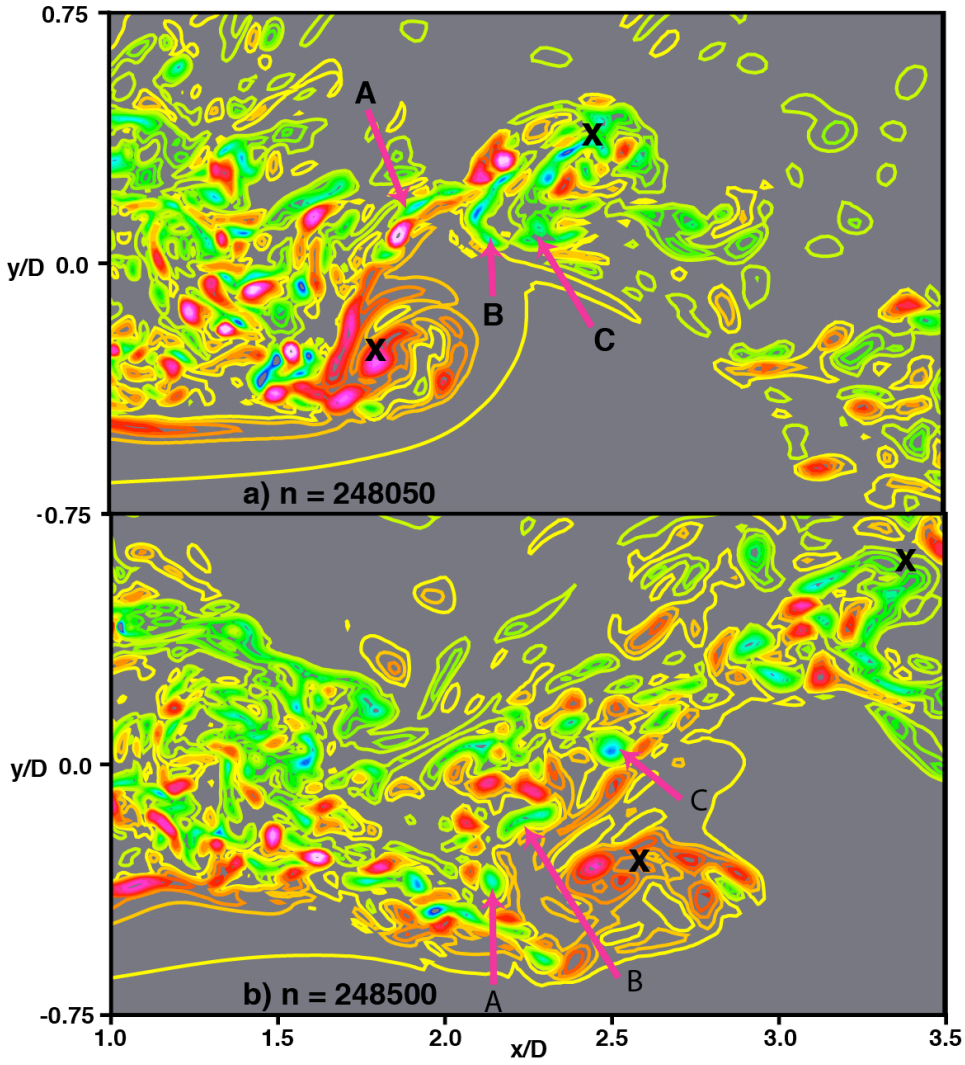

Figure 6. Contours of instantaneous spanwise vorticity for Case TL showing constituent regions of negative spanwise vorticity at a) time step n = 248050 & b) time step = 248500; red/magenta represent high/highest positive values, green/blue low/lowest negative values, yellow ≈ 0.0.

A comparison of the UNSV related contours in Figs. 6a and 6b shows both weakening and distortion of the UNSV. These effects are also evident in the contours of phase-averaged spanwise vorticity in Fig. 4c. The UNSV is far from circular and much weaker than obtained in Case TT. The powerful rotational flow of the LPSV both shears the UNSV downstream of it and draws it closer to itself. This results in an uneven spacing of the shed vortices (the UNSVs in Case TL do not occur close to the midpoint between two successive LPSVs as in Case TT). It should be noted that the UNSV also accumulates constituent regions off positive vorticity from the braid and the upstream LPSV but is less effective in this process. While the acquisition discussed thus far increases contamination of the shed vortices, decontamination is also possible; for example, acquisition of the positive constituent regions of vorticity from the UNSV by the LPSV. This is expected to be a secondary effect since the primary constituents of the UNSV are regions of negative vorticity.

Since Figs. 6a & 6b only provide information at specific instants in time, we next explore the extent of contamination in a phase-averaged sense. The phase-averaged positive and negative spanwise vorticity components $<\Omega_z^{\pm}>$ are defined as follows:

$$<\Omega_z^{\pm}> = <\Omega_z \pm |\Omega_z|> / 2 \qquad (6)$$

The sum of the two components yields the conventional phase-averaged spanwise vorticity. Figures 7a and 7b show contours of the positive and negative components (Case TL), respectively, when the LPSV is at the location x/D = 7.2. Figure 7c shows the sum of the two components. The deep incursion of $<\Omega_z^->$ into the region occupied by the LPSV at x/D = 7.2 is evident. There is a peak value of $<\Omega_z^->$ at the location marked with an 'O' in Fig. 7b. This peak is located below the core of the LPSV, thus further emphasizing the transport of negative vorticity below the centerline.

In a similar fashion the transport of positive vorticity above the centerline (albeit weaker) is seen in Fig. 7a. Here there is a peak in $<\Omega_z^+>$ but upstream of the UNSV (also marked with an 'O', UNSV core occurs downstream of x/D = 8.0 and does not appear in the figure). It is evident from Figs. 7a & 7b that the upward transport of $<\Omega_z^+>$ is weaker than the downward transport of $<\Omega_z^->$. The ratio of the magnitudes of these two 'acquired' peaks at the points marked with an 'O' (lower negative to upper positive) is 1.36. This indicates that the LPSV acquires more negative vorticity than the UNSV acquires positive vorticity.

There are two reinforcing effects to be considered at this point. One is the weakening of both vortices because of the acquisition of vorticity of the opposite sign. The second is the weakening of each vortex caused by the loss of vorticity of its own sign. Figure 7 and the ratio 1.36 provided above indicate that the second effect is the dominant one on the UNSV in Case TL. Contamination has a lesser effect on the LPSV (since it is stronger) than loss has on the UNSV. There is also the possibility that because the UNSV is weaker at inception, even the smaller amount of contamination it absorbs is sufficient to weaken it considerably as it travels downstream. Overall, the combined effects of vorticity loss and vortex contamination (related phenomena), and weakness at inception, results in a much weaker upper vortex than the lower one (a factor of 3.5 in peak phase-averaged spanwise vorticity at x/D = 5.5).

The constituent regions of vorticity A, B & C in Figs. 6a & 6b are not acquired by the LPSV directly from the UNSV but via the braid connecting the two. A consequence of many such transfers contributes to the high levels of $<\Omega_z^->$ in the braid region seen in Fig. 7b (and also the elevated levels of $<\Omega_z^+>$ in the braid in Fig. 7a). However, as discussed in Rai (2015) the assimilation of the log-layer eddies by the braids (and shed vortices) also contributes to the accumulation of vorticity in the braids. In

addition, there is the strengthening of spanwise vortical disturbances in the braid as a result of fluctuating strain rates (Rai 2013).

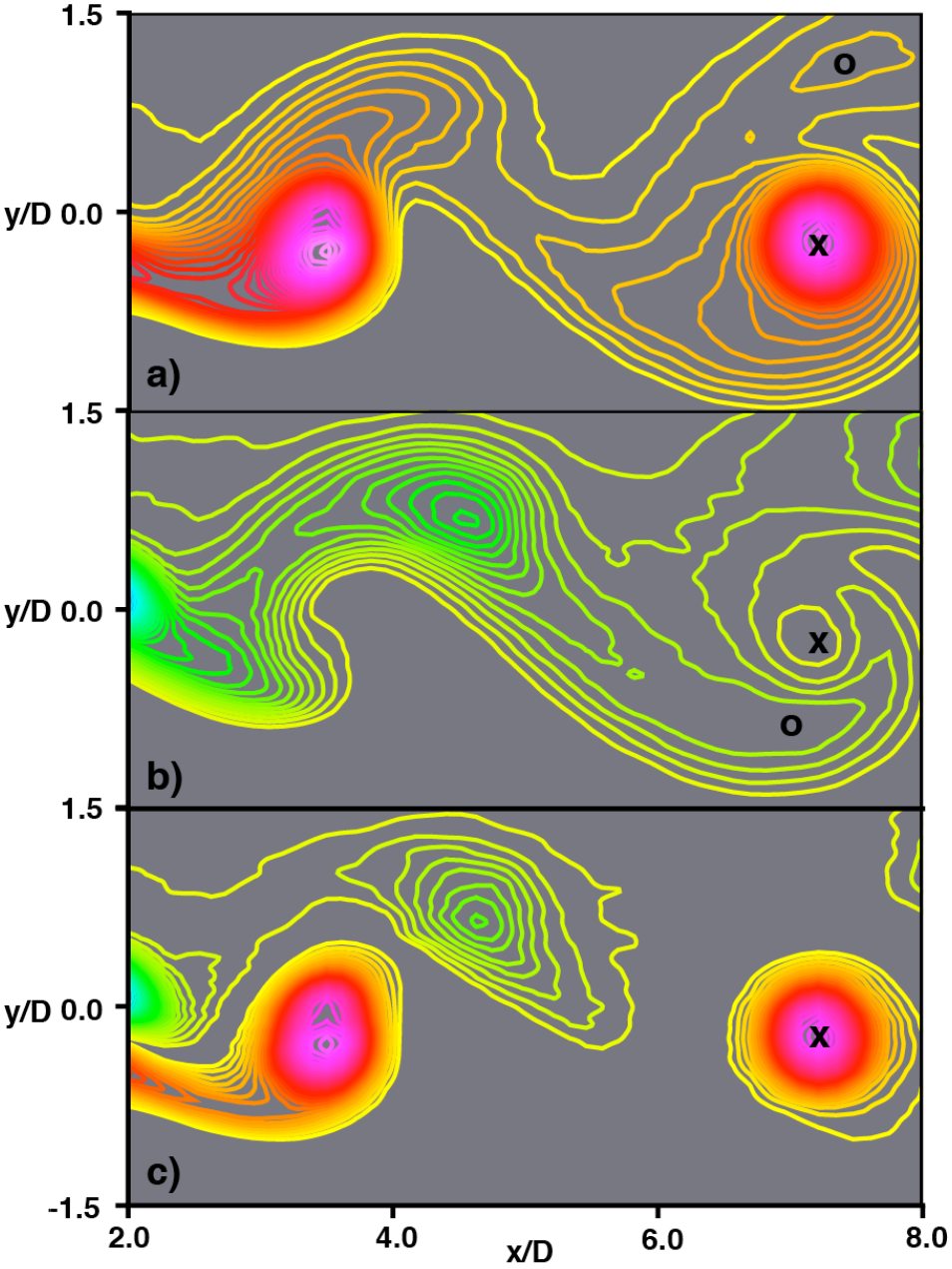

Figure 7. Contours of phase-averaged spanwise vorticity for Case TL, 'X' marks the location of the lower positive vortex of interest at x/D = 7.2: a) $<\Omega_z^+>$, b) $<\Omega_z^->$ & c) $<\Omega_z>$; red/magenta represent high/highest positive values, green/blue low/lowest negative values, yellow ≈ 0.0.

A Comparison of Phase-Averaged Velocity Statistics

In this section differences in the distribution of the phase-averaged normal intensities and shear stress (random component) in Cases TT & TL, and the important contributors to these differences are explored. Contours of the phase-averaged streamwise normal intensity $<u'u'>$ for Case TT when the lower vortex is located at x/D = 4.98 (vortex positions marked with an 'X' in this and the following figures)

are shown in Fig. 8a. Of interest are the peaks near the vortex cores and in the braid regions (braid regions are indicated with an arrow). The entire braid region shows elevated levels of $<u'u'>$. As discussed in Rai (2013), the higher levels of $<u'u'>$ in the braid region are a result of powerful rib vortices in this region. The peaks near the vortex cores are discussed below.

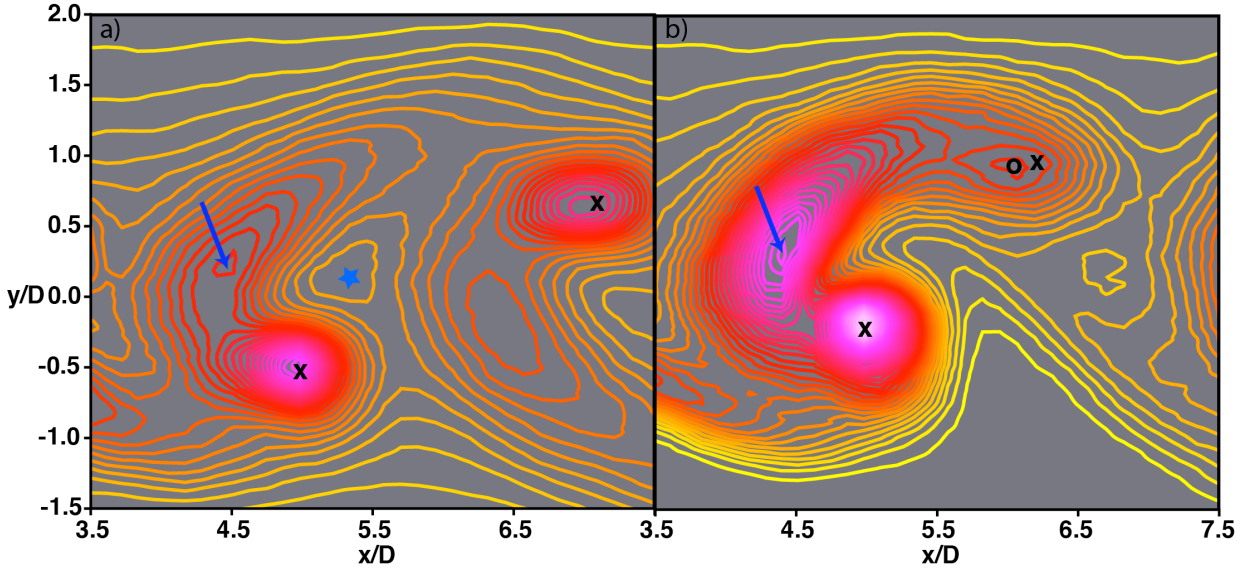

Figure 8. Contours of $<u'u'>$: a) Case TT and b) Case TL, 'X' marks the location of consecutive vortices of interest; red/magenta represent high/highest positive values, yellow ≈ 0.0.

Figure 8b shows contours of $<u'u'>$ for Case TL (lower vortex again at x/D = 4.98). Clearly both the lower-shed-vortex and braid region peaks are much higher in Case TL than in Case TT. The ratio of lower-core-vortex related peak values is approximately 1.4 (TL to TT). The upper vortex core is in closer proximity to the lower one in Case TL than in Case TT. The peak associated with this upper core in Case TL (marked with an 'O' in Fig. 8b) is much weaker than the lower one (ratio of 0.37, upper to lower). It is also weaker than upper-vortex-core related peak of Case TT (ratio of 0.67, TL to TT).

To better understand the observed distributions of $<u'u'>$ we turn to the production term in the transport equation for this term. Figures 9a & 9b show contours of the turbulence production term P_{11} in the budget of $<u'u'>$ for Cases TT & TL, respectively. As in the case of phase-averaged vorticity, the production term (and other budget terms presented later in the text) has been filtered with a three-point filter to reduce high-frequency oscillations in the contours. In addition, here and in the following contours plots, the contour corresponding to the value zero has been omitted to clearly demarcate positive/negative regions. The production term is given by (Eqs. 3 & 4),

$$P_{11} = -2\rho\left[<u'u'>\frac{\partial<u>}{\partial \mathrm{x}} + <u'v'>\frac{\partial<u>}{\partial \mathrm{y}}\right] \qquad (7)$$

The term $<u'w'>\partial<u>/\partial z$) does not appear in Eq. 7 (homogeneity in the z direction). The braid region shows significant turbulence production and contains a local maximum in production in both cases. These two features are consistent with those seen in Fig. 8 (high intensity in the braid with a local maximum). The braids emanating from the cores first move upstream and then downstream. In the region where they turn the braids and the rib vortices contained within them have a large cross-stream vorticity component thus resulting in large values of u' and a maximum in $<u'u'>$. The rib vortices are also subject to stretching by the phase-averaged strain rate caused by the two shed vortices at the ends of the braid.

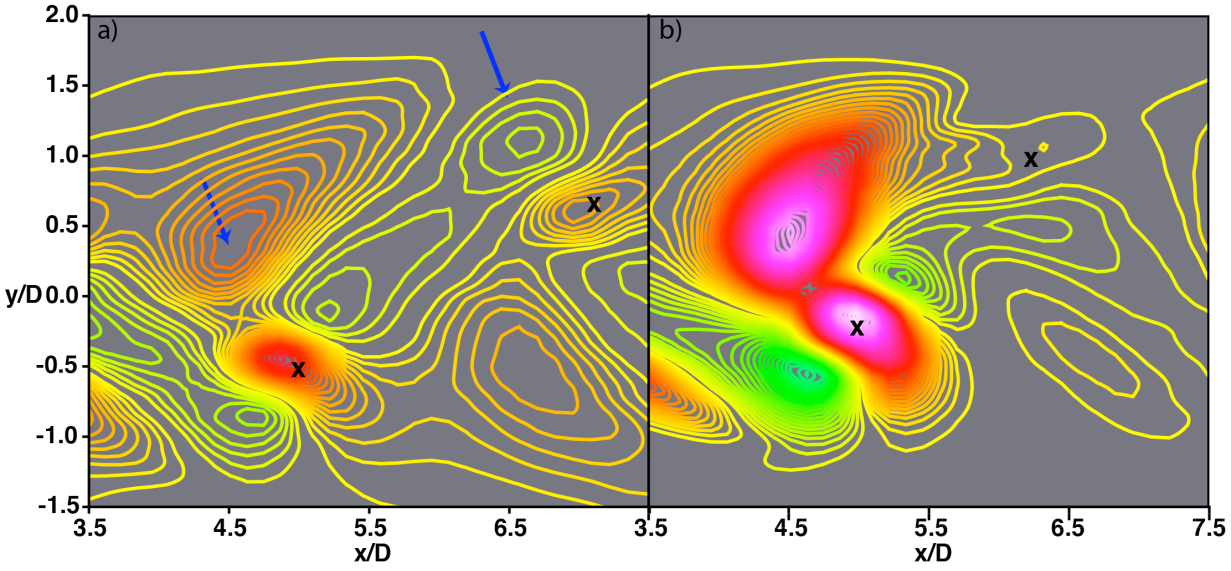

Figure 9. Contours of the production term P_{11} with lower vortex core at x/D = 4.98:
a) Case TT and b) Case TL, 'X' marks the location of consecutive vortices of interest; red/magenta represent high/highest positive values, green/blue low/lowest negative values, yellow ≈ 0.0.

The lower vortex cores show a positive production rate that is consistent with the maximum in intensity that exists in the core. As mentioned in Rai (2013), in the vicinity of the vortex cores the contour lines of $< u >$ are essentially horizontal and densely packed in the vertical direction, thus yielding small values of the x-derivative and large values of the y-derivative of $< u >$. The second term in the equation for P_{11}, containing the shear stress, is thus the dominant one. Since for the vortices below the centerline the velocity derivative is negative and $< u'v' >$ is positive (see Fig. 19), P_{11} in these vortex cores is positive (similar reasoning applies to the upper cores). In fact a maximum occurs near each vortex core. Physically, the presence of spanwise elongated segments of spanwise vorticity and, segments of rib vortices contained within the core and aligned with it both result in high values of $< u'u' >$ and a local maximum in the core (Rai, 2013).

Figures 9a & 9b provide a better understanding of the relative values of the maxima in $< u'u' >$ in Figs. 8a & 8b. For example, the ratio of the maxima of P_{11} at the lower cores of Cases TT and TL is 2.3 (TL to TT); this is consistent with the higher value of $< u'u' >$ at the lower vortex core of Case TL. In addition the peak value of P_{11} associated with the upper vortex in Case TL in Fig. 9b is very low and is thus consistent with the correspondingly lower peak in $< u'u' >$ in Fig. 8b. However, it is not only the production term that determines the distributions of $< u'u' >$ seen in Fig. 8; the other budget terms of Eqs. 3 & 4 also play important roles. The transport, dissipation and velocity pressure-gradient terms are discussed shortly.

The core related peaks in $< u'u' >$ in Case TT are essentially constant in the region 3.5 < x/D < 4.75 and subsequently decrease with increasing x/D (braid related peaks decrease continuously from x/D = 3.5). Cores and braids that are well defined first appear at about x/D = 2.5 (Rai, 2014); the first 3.5 diameters are roughly the formative region in this case. However, Case TL exhibits a different evolution of $< u'u' >$ as the shed vortices travel downstream. Figures 10a -10d show $< u'u' >$ distributions for Case TL when the lower vortex is at the locations x/D = 3.50, 4.98, 7.21 & 9.55, respectively.

It is clear from these figures that while the braid related peak decreases with increasing x/D, the lower-vortex-core related maximum first increases and then decreases with increasing x/D. This of course

can be interpreted as Case TL possessing an extended formative region where the basic topological features of the $<u'u'>$ distribution remain the same but the magnitudes are in considerable flux.

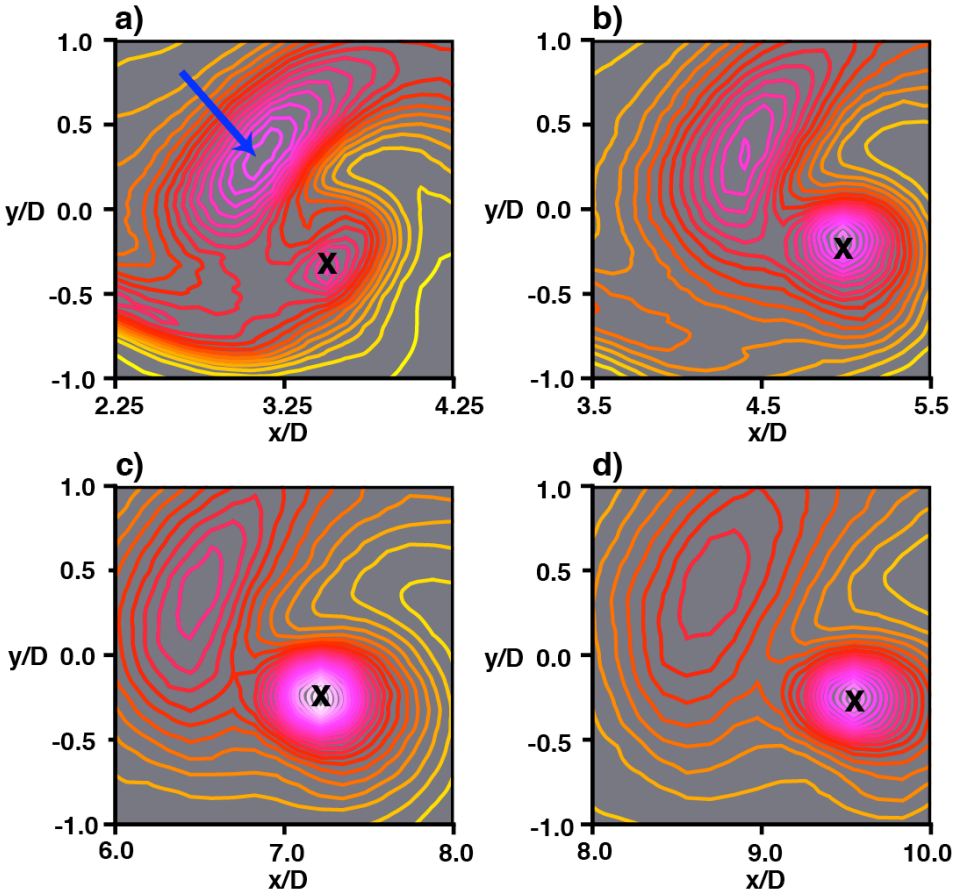

Figure 10. Contours of $<u'u'>$ for Case TL with vortex cores at (marked with an 'X') a) x/D = 3.50, b) x/D = 4.98, c) x/D = 7.21 & d) x/D = 9.55; red/magenta represent high/highest positive values, yellow ≈ 0.0.

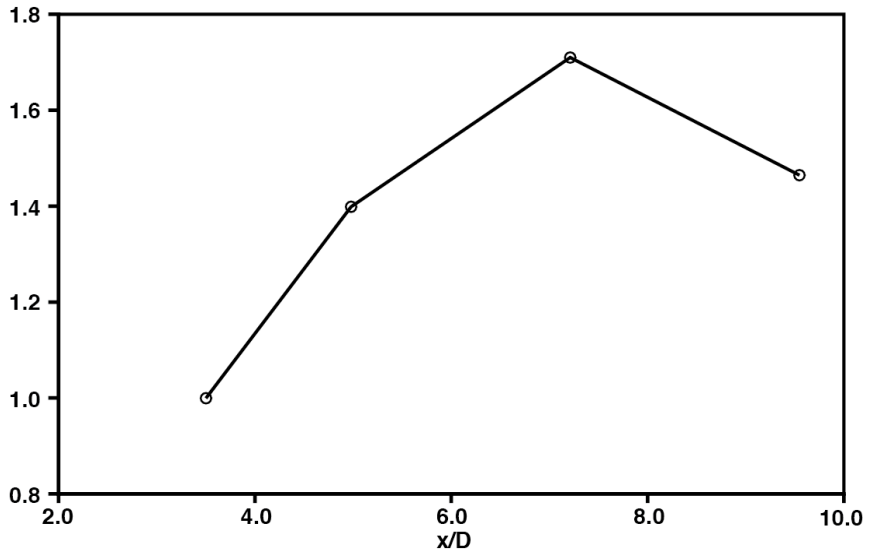

Figure 11. Variation of lower-vortex-core related peak in $<u'u'>$ with x/D, Case TL.

Figure 11 shows the variation of the core-related peak value of $<u'u'>$ at the four streamwise stations of Fig. 10 (normalized by the peak value at x/D = 3.5). The value at x/D = 7.21 is about 1.7 times larger than at x/D = 3.5 and decreases thereafter. In the following, some of the reasons underlying this surprising evolutionary behavior, in the lower-core related peak value of $<u'u'>$ in Case TL, are explored. In the process the distributions of the budget terms in the two cases are discussed and compared.

Figures 12a and 12b show the distributions of the transport term T_{11} in the budget for $<u'u'>$ in Cases TT & TL, respectively. As in Fig. 8, the lower vortex core is at x/D = 4.98 in both figures. In Fig. 12a the braid region shows three distinct layers. The transport term is negative in the middle layer and positive in the two outer layers indicating transport of $<u'u'>$ out of the relatively higher intensity middle layer into the lower intensity outer layers. The core regions show a central negative minimum and two peripheral positive maxima, again indicating transport of $<u'u'>$ from the core to the two low intensity regions located above and below the core seen in Fig. 8 (the star in Fig. 8a is at a local minimum in intensity). The distribution of the transport term in Fig. 12a is not surprising; it reflects the distribution of $<u'u'>$.

While the braid related layers are present in Fig. 12b as well, the vortex core region is markedly different than in Fig. 12a. The inner core shows a *positive* maximum for T_{11}, which contributes to further strengthening of $<u'u'>$ in the inner core. This maximum is flanked by two negative minima (blue arrows). The ratio of the upstream minimum value of T_{11} to the core minimum in Fig. 12a is about 1.3. The corresponding ratio for the downstream minimum in Fig. 12b is 0.9. Both ratios are less than the ratio obtained for production in the core (2.3, TL to TT, as stated earlier). Thus, Case TL does not exhibit a proportionately higher transport rate of $<u'u'>$ out of the core region. This is one of the contributing factors to the increasing value of lower-core related $<u'u'>$ for about four diameters of vortex travel downstream (Figs. 10 & 11). Further downstream, the distribution of T_{11} in Case TL, in the lower core region is very similar to that obtained in Case TT in Fig. 12a. This feature is consistent with the decrease seen in peak $<u'u'>$ in Fig. 10. The upper core in Fig. 12b does show a negative minimum in its vicinity as in Fig. 12a. The ratio of peak negative transport values associated with the upper cores in Figs. 12a & 12b is about 0.8 (TL to TT). This again is consistent with the weaker upper vortex in Case TL.

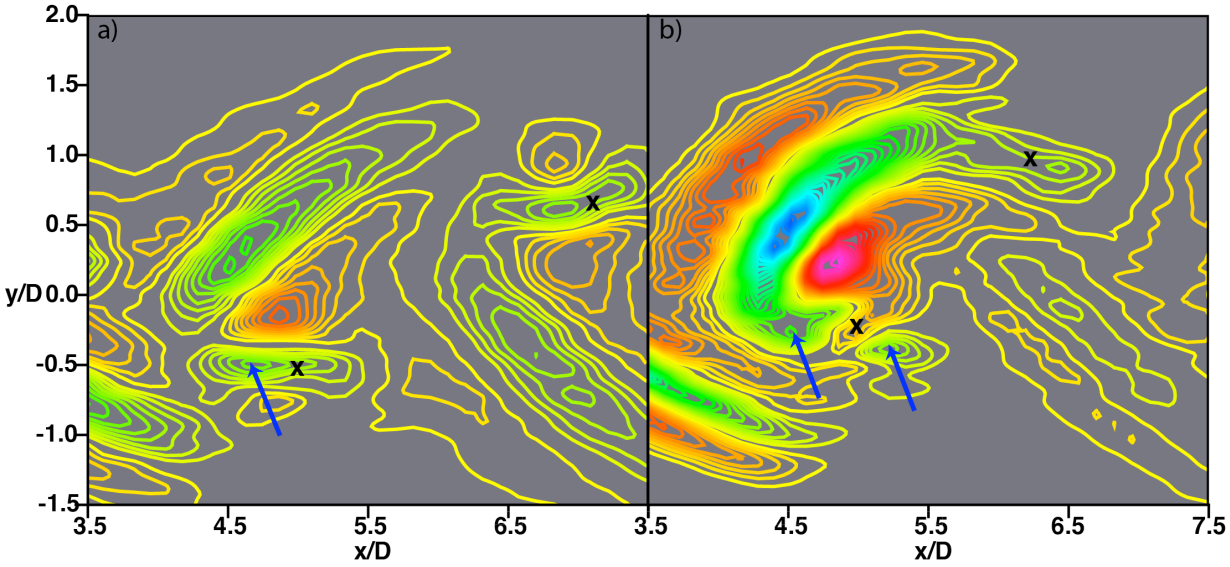

Figure 12. Contours of the transport term T_{11} with lower vortex core at x/D = 4.98:
a) Case TT and b) Case TL, 'X' marks the location of consecutive vortices of interest; red/magenta represent high/highest positive values, green/blue low/lowest negative values, yellow ≈ 0.0.

Figures 13a & 13b show the distributions of the dissipation term ε_{11} in the budget for $<u'u'>$ in Cases TT & TL, respectively. The lower vortex core is at x/D = 4.98 in both figures. Both the braids and cores in Fig. 13a, Case TT, show high levels of dissipation with a maximum near each core. Case TL, in Fig. 13b, also shows the same general attributes. The peak associated with the upper core is not apparent in Fig. 13b. A significantly larger number of contours show a maximum slightly to the left of this core. More importantly, the ratio of peak dissipation rates in the lower cores is 1.35 (TL to TT). Hence, the dissipation rate in Case TL is not proportionately higher (the peak production rate in Case TL is 2.3 times higher). Thus, the *relatively lower* turbulent dissipation rate ε_{11} (relative to the increase in production) is also a contributing factor to the increase in the lower-core related peak value of $<u'u'>$ in Case TL seen in Figs. 10 & 11.

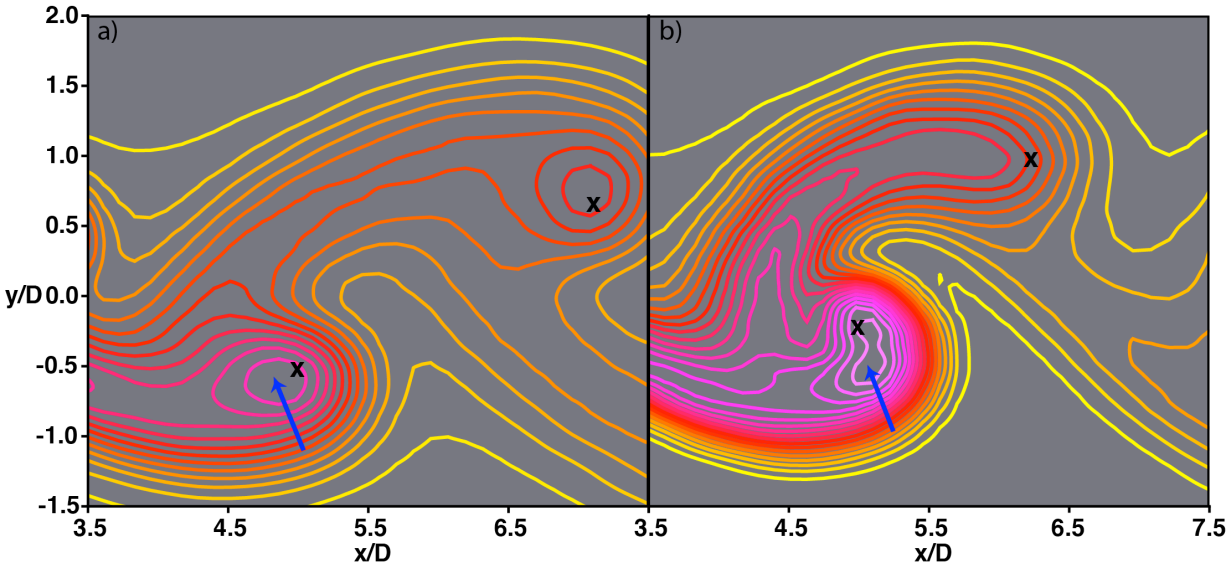

Figure 13. Contours of the dissipation term ε_{11} with lower vortex core at x/D = 4.98:
a) Case TT and b) Case TL, 'X' marks the location of consecutive vortices of interest; red/magenta represent high/highest positive values, yellow ≈ 0.0.

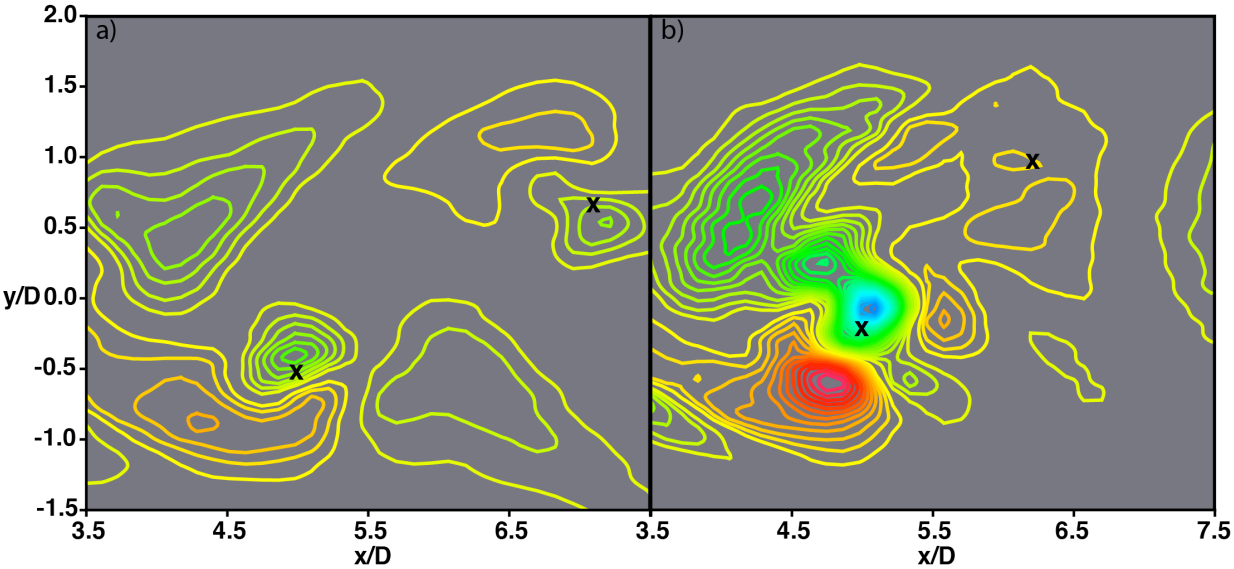

Figure 14. Contours of the velocity pressure-gradient term π_{11} with lower vortex core at x/D = 4.98:
a) Case TT and b) Case TL, 'X' marks the location of consecutive vortices of interest;
red/magenta represent high/highest positive values, green/blue low/lowest negative values, yellow ≈ 0.0.

Figures 14a & 14b show contours of the velocity pressure gradient term π_{11} in cases TT & TL, respectively. The center of the vortex in both cases is embedded in a region of negative π_{11} (leading to a reduction of $<u'u'>$ with vortex travel). The negative peak obtained in Case TL is higher than that obtained in Case TT by a factor of 3.22. This ratio is greater than the factor of 2.3 obtained for the production term. This of course raises the following question: is the magnitude large enough to compensate for the relatively lower transport and dissipation rates obtained in Case TL? The answer lies in the distribution of the combined contribution of all the budget terms (right hand side of Eq. 3, term R_{11}).

Contours of the term R_{11} for the cases TT and TL are provided in Figs. 15a & 15b. The nearly circular core region of the lower vortex in Fig. 15a consists of four lobes. The lobes closely correspond to the four quadrants (Q1, Q2, Q3 & Q4) of this circular region. R_{11} is largely negative in quadrants Q1 & Q3 (with associated negative peaks) and it is largely positive in quadrants Q2 & Q4 with corresponding positive peaks. The center of the vortex shows a slightly positive value of R_{11}; more importantly the location of peak $<u'u'>$, indicated with a star (magenta), is in a region of negative R_{11}. This is consistent with the peak value of $<u'u'>$ decreasing as the vortex travels downstream. We note that the negative contours are the ones that are continuous through the central region (a negative pathway). As expected the upper vortex located further downstream shows a very similar pattern of lobes. The braid region connecting the two cores shows mostly negative values of R_{11}. Figure 16 shows a superimposition of contours of R_{11} (Fig. 15a) on contours of $<u'u'>$ (Fig. 8a).

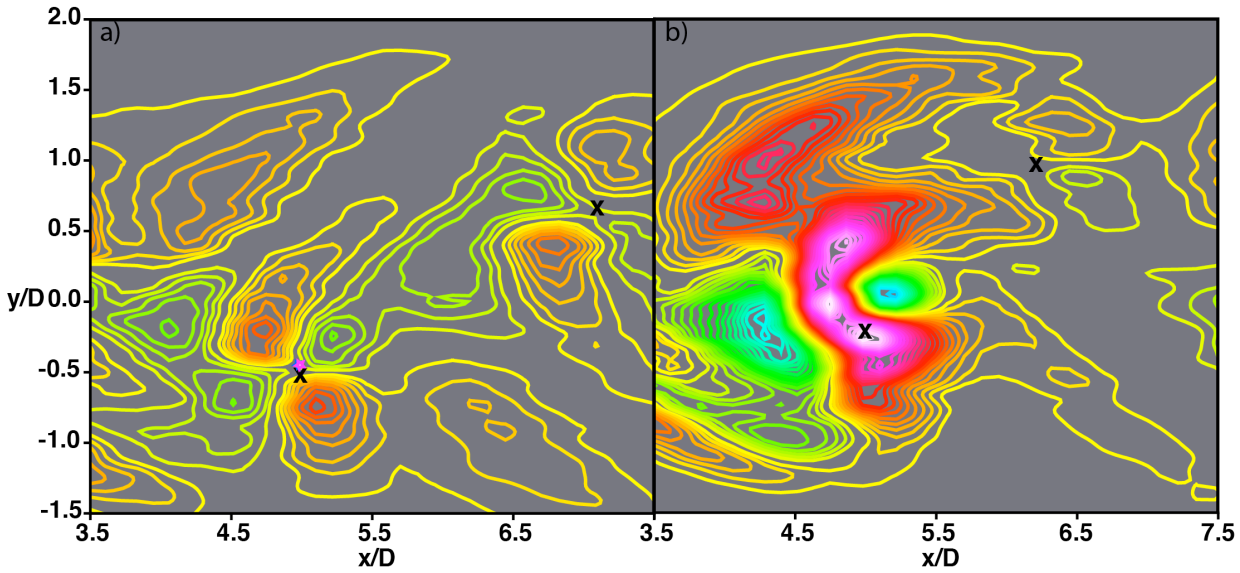

Figure 15. Contours of the term R_{11} with lower vortex core at x/D = 4.98:
a) Case TT and b) Case TL, 'X' marks the location of consecutive vortices of interest;
red/magenta represent high/highest positive values, green/blue low/lowest negative values, yellow ≈ 0.0.

In Case TL both the center of the vortex and the peak in $<u'u'>$ (the peak almost coincides with the center as can be seen in Fig. 8b) are both located in a region where the term R_{11} is positive. In fact the core nearly coincides with a positive peak in R_{11}. This is consistent with the rapid increase in peak $<u'u'>$ observed in Figs. 10 & 11. In Case TL the distribution of R_{11} is in a state of considerable flux. When the core is at x/D = 9.55 as in Fig. 10d, the peak in $<u'u'>$ is located in a region of negative R_{11} as in case TT (Fig. 15a) and this is consistent with the decrease in $<u'u'>$ seen at this streamwise location (Figs. 10d & 11). Although much of the discussion has focused on the vortices, a portion of the braid with the related peak in both cases (with lower vortex cores at x/D = 4.98) is located in a region of negative R_{11}, and that is consistent with the observed decrease in these peaks with increasing x/D.

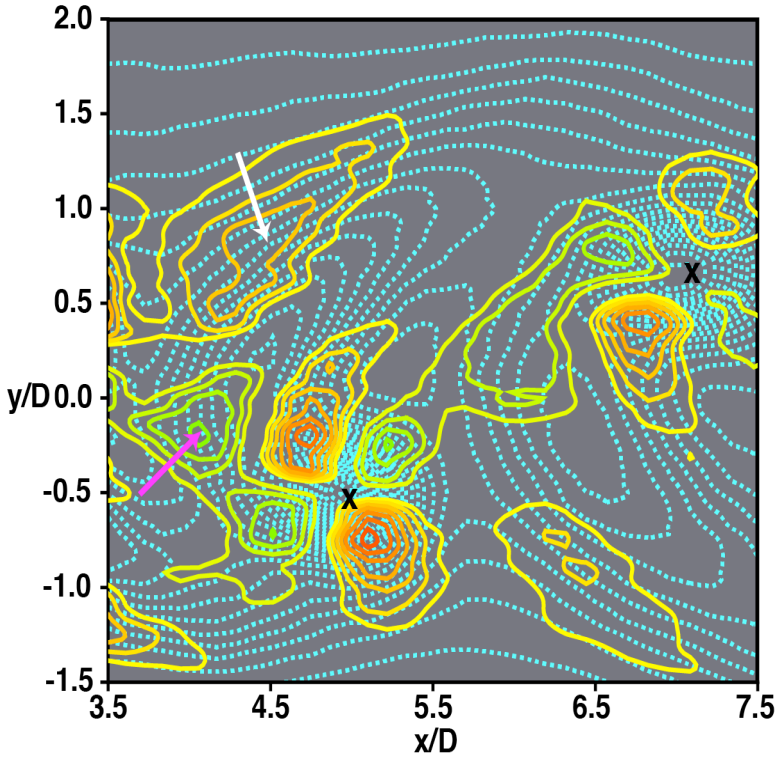

Figure 16. Contours of R_{11} from Case TT (Fig. 15a, vortex core at x/D = 4.98) superimposed on contours of $<u'u'>$ (dashed light blue contours, from Fig. 8a);
red/magenta represent high/highest positive values, green/blue low/lowest negative values, yellow ≈ 0.0.

Figure 17a & 17b shows contours of $<u'u'>$ obtained at x/D = 4.98 & 10.99 in Case TT. There are a few features of interest to be noticed in these two figures.

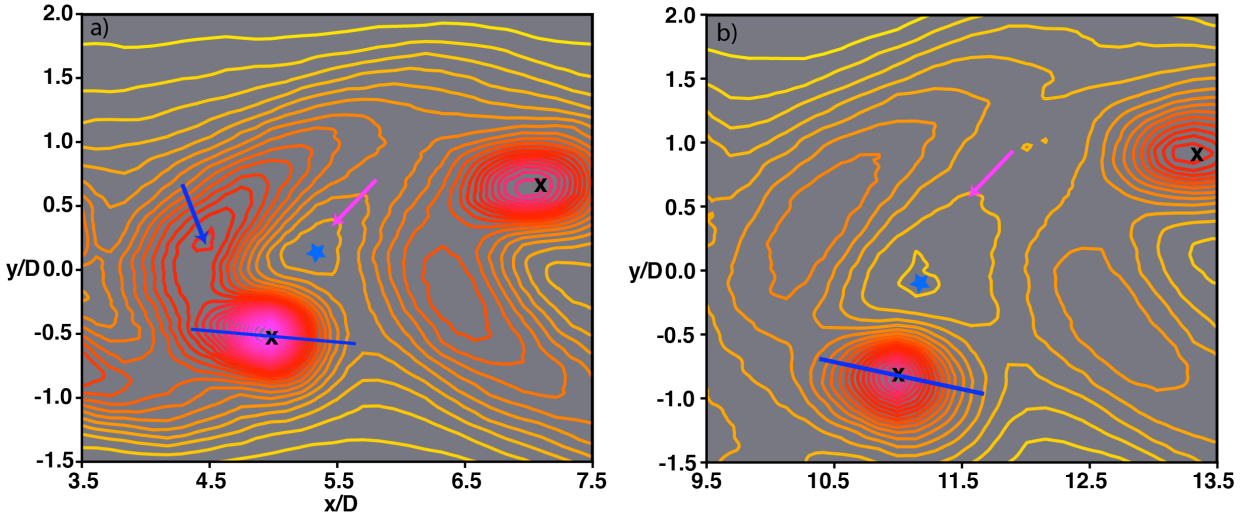

Figure 17. Contours of $<u'u'>$ for Case TT with lower vortex cores located at a) x/D = 4.98 and b) X/D = 10.99, 'X' marks the location of consecutive vortices of interest; red/magenta represent high/highest positive values, yellow ≈ 0.0.

Firstly, the region of core-related high $<u'u'>$ changes from nearly circular to an elliptic shape with the major axis tilted at a small angle away from the centerline (see blue line in Figs. 17a & 17b). This is consistent with the four-lobed pattern of R_{11} seen in Fig. 15a and Fig. 16 (signs included). The region containing the minimum shown with a magenta arrow (minimum located at blue star) is much larger at x/D = 10.99 and the positive minimum value itself is lower by a factor of 1.35 at x/D = 10.99. This is consistent with the region of negative R_{11} corresponding to Q1 and the braid region connecting the two cores (Fig. 16). The peak in $<u'u'>$ within the braid region decreases with increasing x/D and is consistent with the region of negative R_{11} (peak of this region of negative R_{11} is shown with a magenta arrow in Fig. 16). The region shown with a white arrow in Fig. 16 has slightly positive R_{11} values and serves to expand the braid region upward and upstream (towards the upper left corner of the plot).

While the discussion above is a fairly extensive description of the distribution of each of the budget terms and R_{11}, and their effect on the evolution of the distribution of $<u'u'>$, it helps in understanding a very complex feature. *The increase in core related peak $<u'u'>$ with increasing x/D in Case TL is a result of rates of dissipation and outbound transport that are not proportionately higher in comparison to the higher rate of production obtained in this case. The increase in peak $<u'u'>$ with increasing x/D occurs in spite of the more than proportionate increase in the magnitude of core related negative velocity pressure-gradient values (comparing cases TT & TL).* The exercise also demonstrates how the budget terms may be used in understanding the evolution of phase-averaged turbulent stresses.

Contours of the phase-averaged cross-stream normal intensity $<v'v'>$ in Cases TT & TL are shown in Figs. 18a &18b. Both the braid and core regions show high levels of $<v'v'>$ with a maximum at each core and a saddle point in each braid. Peak values of $<v'v'>$ decrease with increasing x/D (for x/D > 3.5) as the vortices travel downstream for both upper and lower vortices in both Cases TT & TL. The reasons underlying the features of the distribution of $<v'v'>$ in Fig. 18a are provided in Rai (2013).

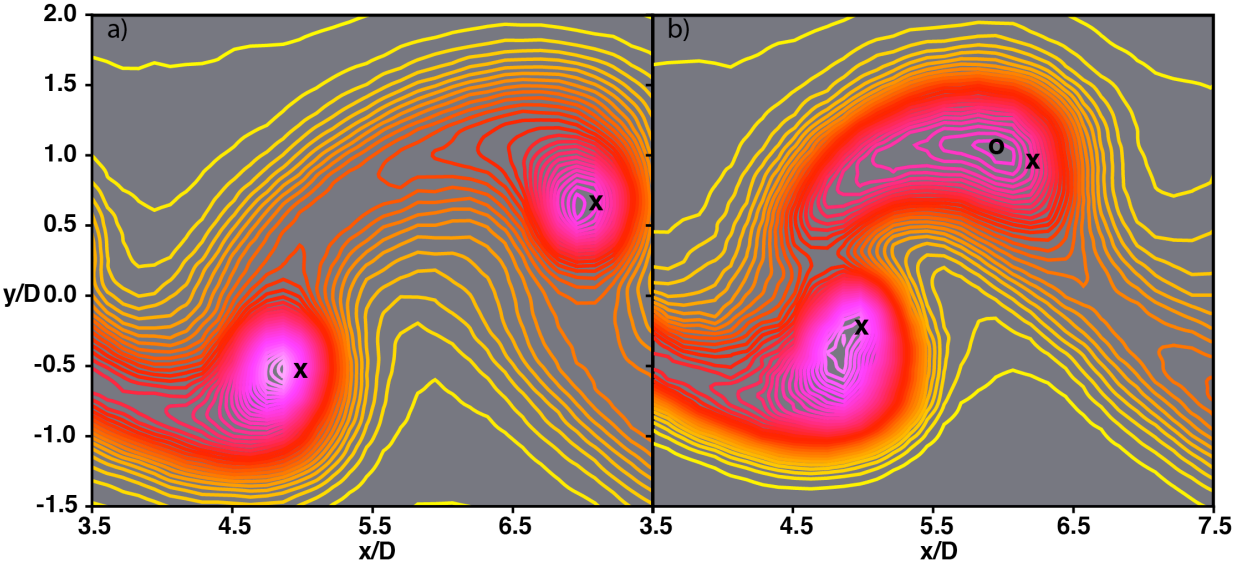

Figure 18. Contours of $<v'v'>$: a) Case TT and b) Case TL, 'X' marks the location of consecutive vortices of interest; red/magenta represent high/highest positive values, yellow ≈ 0.0.

Contours of the phase-averaged shear stress $<u'v'>$ in Cases TT & TL are shown in Figs. 19a &19b (same lower vortex locations as in Fig. 8). As expected the distribution is largely negative above the centerline and positive below it. Both the braids and vortex cores show elevated levels of $<u'v'>$. The

braid regions both above and below the centerline in both cases show a peak. Peak values also exist in the lower core regions in both cases TT & TL and in the upper core of Case TT. The upper core of Case TL does not possess a peak. We note here that the minimum and maximum contour levels and the number of contours in Figs. 8, 18 & 19 are the same. The distributions of the budget terms for $<v'v'>$ and $<u'v'>$ are not included here but do provide an understanding of the distributions of these turbulent stresses. The reasons for the distribution of $<u'v'>$ seen in Fig. 19a, including an explanation based on the production term P_{12} are provided in Rai (2013).

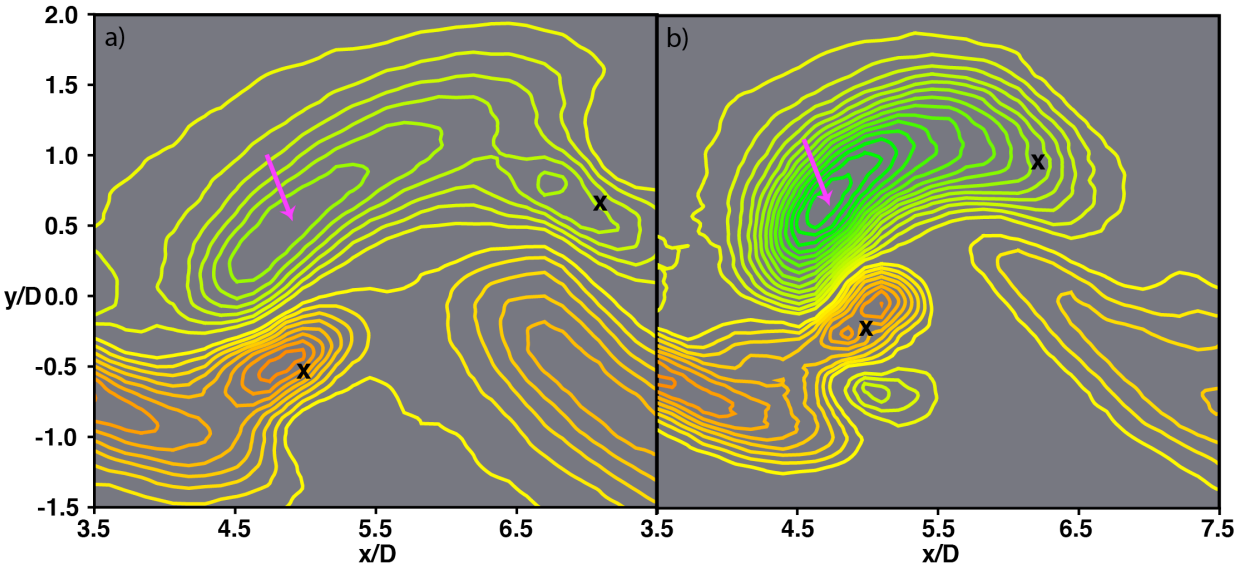

Figure 19. Contours of $<u'v'>$: a) Case TT and b) Case TL, 'X' marks the location of consecutive vortices of interest; red/magenta represent high/highest positive values, green/blue low/lowest negative values, yellow ≈ 0.0.

The distributions of normal intensity, shear stress and budget terms provided in this section show the differences in the dynamics of the symmetric and asymmetric cases and may prove to be useful in accurately modeling wake turbulence.

CONCLUDING REMARKS

This investigation focuses on the near wake of a flat plate. Two cases are investigated here; the first is a symmetric wake, where both the upper and lower boundary layers are turbulent and statistically the same, and the second is an asymmetric wake where the upper boundary layer is turbulent and the lower one is laminar. Direct numerical simulations of these cases were performed with a high-order accurate upwind biased scheme. The objective here is to investigate the evolution of the wakes in the two cases in the region x/D < 13.0. The focus is on shed-vortex structure/evolution and phase-averaged velocity statistics. The two wakes are explored with the aid of contours of instantaneous and phase-averaged spanwise vorticity, and contours of phase-averaged turbulence intensities and shear stress and the budget terms in the corresponding transport equations.

Phase-averaged contours of spanwise vorticity showed that in the asymmetric case peak vorticity in the upper vortex core was a factor of 1.27 smaller than in the lower vortex core at inception. This factor grows to 3.45 at the location x/D = 5.5. In addition, the lower vortex core in this case has a peak vorticity value 1.21 times greater at inception than obtained in Case TT. These effects are explained here via

processes such as DSL fragmentation, vortex contamination and the extent of the upstream boundary layer that participates in the formation of the shed vortex. One of the primary causes underlying the extreme weakening of the upper shed vortex in Case TL is the loss of negative vorticity to, and acquisition of positive vorticity from, the lower shed vortex. This process starts at vortex inception and continues as the vortices travel downstream. In a phase-averaged sense the upper vortices are sheared (not nearly circular as the lower ones) and are closer to the upstream lower vortex instead of midway between two lower vortices as in Case TT.

The distributions of phase-averaged intensities and shear stress (random component) in the two cases are also examined here and compared. One striking difference between the two cases is that in Case TL there is a rapid increase in the core-related peak value of $<u'u'>$ between x/D = 3.5 and 7.2 followed by a fairly rapid decrease thereafter. The core related peak in $<u'u'>$ in Case TT is essentially the same for 3.5 < x/D < 4.75 and subsequently decreases with increasing x/D. This difference between the two cases was studied extensively via the budget terms in the transport equation for $<u'u'>$. It was found that the turbulent production rate in the region of interest was substantially higher in Case TL. The increase in peak $<u'u'>$ with increasing x/D in Case TL is a result of rates of dissipation and transport that are not proportionately higher in comparison to the increase in the rate of production (notwithstanding the more than proportionate increase in the magnitude of core related velocity pressure-gradient values in Case TL). The exercise also demonstrates how, in general, the budget terms may be used in understanding the evolution of phase-averaged turbulent intensities and shear stress. Differences in the distributions of $<v'v'>$ and $<u'v'>$ in the two cases are also discussed.

REFERENCES

CHEVRAY, R. & KOVAZNAY, L. S. G. 1969 Turbulence measurements in the wake of a thin flat plate. *AIAA Journal*, Vol. 7, 1641.

HAH, C., and LAKSHMINARAYANA, B. 1982 Measurement and prediction of mean velocity and turbulence structure in the near wake of an airfoil. *Journal of Fluid Mechanics*, Vol. 115, 251.

HAYAKAWA, M. & Iida, S. –I. 1992 Behavior of turbulence in the near wake of a flat plate at low Reynolds number. *Physics of Fluids A*, Vol. 4 (10) 2282.

MANSOUR, N. N., KIM, J. & MOIN, P. 1988 Reynolds-stress and dissipation-rate budgets in a turbulent channel flow. *Journal of Fluid Mechanics,* Vol. 194, 15.

NAKAYAMA, A. & LIU, B. The turbulent near wake of a flat plate at low Reynolds number. *Journal of Fluid Mechanics*, Vol. 217, 93.

RAI, M. M. 2012 Phase-averaged Reynolds-stress budget in the turbulent near wake of a flat plate. Paper 2012-0067, 50th AIAA Aerospace Sciences Meeting, Nashville, Tennessee.

RAI, M. M. 2013 Flow physics in the turbulent near wake of a flat plate. *Journal of Fluid Mechanics*, Vol. 724, 704.

RAI, M. M. 2014 Flow Phenomena in the very near wake of a flat plate with a circular trailing edge. *Journal of Fluid Mechanics*, Volume 756, 510.

RAI, M. M. 2015 Detached shear-layer instability and entrainment in the wake of a flat plate with turbulent separating boundary layers. *Journal of Fluid Mechanics*, Vol. 774, 5.

RAMAPRIYAN, B. R., PATEL, V. C. & SASTRY, M. S. 1982 The symmetric turbulent wake of a flat plate. *AIAA Journal*, Vol. 20 (9), 1228.

REYNOLDS, W. C. & HUSSAIN, A. K. M. F. 1972 The mechanics of an organized wave in turbulent shear flow. Part 3. Theoretical models and comparisons with experiments. *Journal of Fluid Mechanics,* Vol. 54, 263.

THOMAS, F. O., and LIU, X. 2004 An experimental investigation of symmetric and asymmetric turbulent wake development in pressure gradient. *Physics of Fluids*, Vol. 16, No. 5, 1725.